Impact of Layer Alignment on the Behavior of MoS_2-ZrS_2 Tunnel Field-Effect Transistors: An *Ab Initio* Study

Anh Khoa Augustin Lu,[1,2,*] Michel Houssa,[1] Mathieu Luisier,[3] and Geoffrey Pourtois[2,4,†]

[1]*Semiconductor Physics Laboratory, Department of Physics and Astronomy, University of Leuven, Celestijnenlaan 200 D, B-3001 Leuven, Belgium*

[2]*IMEC, 75 Kapeldreef, B-3001 Leuven, Belgium*

[3]*Integrated Systems Laboratory, ETH Zürich, CH-8092 Zürich, Switzerland*

[4]*Department of Chemistry, Plasmant Research Group, University of Antwerp, B-2610 Wilrijk-Antwerp, Belgium*

(Received 7 February 2017; revised manuscript received 20 June 2017; published 22 September 2017)

Tunnel field-effect transistors based on van der Waals heterostructures are emerging device concepts for low-power applications, auguring sub-60 mV/dec subthreshold swing values. In these devices, the channel is built from a stack of several different two-dimensional materials whose nature allows tailoring the band alignments and enables a good electrostatic control of the device. In this work, we propose a theoretical study of the variability of the performances of a MoS_2-ZrS_2 tunnel field-effect transistor induced by fluctuations of the relative position or the orientation of the layers. Our results indicate that although a steep subthreshold slope (20 mV/dec) is achievable, fluctuations in the relative orientation of the ZrS_2 layer with respect to the MoS_2 one lead to a significant variability in the tunneling current by about one decade. This arises from changes in the orbital overlap between the layers and from the modulation of the transport direction.

DOI: 10.1103/PhysRevApplied.8.034017

I. INTRODUCTION

The reduction of the physical dimensions of the complementary metal-oxide-semiconductor transistors has been leading to a continuous performance degradation accompanied with an increase in power consumption [1,2]. Since silicon is gradually reaching its intrinsic limits in terms of scaling capabilities, new materials are being investigated as potential replacement candidates in the transistor channel. Among them, two-dimensional (2D) materials [3] are one the most promising class of materials that have the potential to further enable the downscaling of the transistor dimensions, thanks to their self-passivating nature and to the promise of an improved electrostatic control [4,5]. Yet, the current building block of nanoelectronics, i.e., the metal-oxide-semiconductor field-effect transistor (MOSFET) is also intrinsically limited in terms of switching performances due to the Fermi-Dirac distribution of the charge carriers, which sets the lowest limit to the subthreshold swing (SS) at 60 mV/decade at 300 K [6]. The approach to reducing the power consumption consists of lowering the supply voltage of the transistor V_{DS}. This, however, sets an intrinsic limit to the *on*:*off* ratio of the drive current and hampers the modulation achievable during the device operation. To circumvent this issue, new device concepts have emerged to filter the energy distribution of the injected electrons and, hence, to allow a steeper switching, with SS values below 60 mV/dec. One of them is the tunnel field-effect transistor (TFET), which relies on band-to-band tunneling current [7–9].

The combination of this concept with 2D materials in a TFET offers the promise of the development of low-power transistors. For this to occur, van der Waals heterostructures [10] could be used, with the constraint that the two underlying materials exhibit a close-to-broken band-gap alignment between their respective valence and conduction bands. Naturally, alternative band alignments can be obtained by tuning the nature of the materials used in the heterostack [11,12]. This concept has been demonstrated by Szabo *et al.* for a $MoTe_2$-SnS_2 heterostructure [13]. However, as the main interlayer interactions are weak van der Waals forces, the active layers in the channel constituting the stack may easily move with respect to each other, which would induce some variability in the control of the layer alignments and, consequently, have an impact on the electronic properties and on the performances of the devices.

In this work, we focus on transition metal dichalcogenides (TMDs), present a theoretical study of the MoS_2-ZrS_2 heterostructure for a TFET application, and analyze how the relative layer alignment impacts the device characteristics. We consider MoS_2 and ZrS_2 in their 2*H* morphology, since recent reports suggest that transitions between the 1*T* and 2*H* morphologies are possible for ZrS_2, for instance with partial hydrogenation [14]. Our results reveal that although this combination of materials is promising for

*augustin.lu@aist.go.jp
†geoffrey.pourtois@imec.be

TFET applications, a variation in the relative position of the layers induces a strong variability on the TFET electrical performances. The modulation of the *on* and *off* currents together with the subthreshold slope of the device originates from the variations induced by the changes in orientation on the orbital overlap between the layers and/or on the transport direction.

II. COMPUTATIONAL DETAILS

The lattice structural properties of the stacked layers are evaluated using first-principles calculations with the optimized Becke 1986 functional (optB86b) exchange-correlation functional [15] and with the Grimme *D*2 correction scheme for the dispersion forces [16], as implemented in the QUANTUM ESPRESSO software package [17]. The cutoff value for the kinetic energy is set to be 60 Ry and the *k*-point grid to a $9 \times 9 \times 1$ Monkhorst-Pack one [18] (a *k*-point density of 0.1 Å^{-1}). This ensures that the total energy is converged within 0.002 eV/atom between two iterations and that the resulting total atomic forces are inferior to 0.005 eV/Å. The core electrons are approximated using the Garrity-Bennett-Rabe-Vanderbilt (GBRV) ultrasoft pseudopotentials [19]. The electronic properties of the MoS_2-ZrS_2 heterostructures have been evaluated using different layer alignments, built by the application of translation and rotation operations of the ZrS_2 monolayer with respect to the MoS_2 one. Given that the lattice parameters of the 2*H* phases of MoS_2 and ZrS_2 are very different (3.14 Å vs 3.53 Å), the creation of a periodic unit cell for the heterostructure requires some adjustments to accommodate the lattice mismatch and the artificial strain induced in the layers, which would otherwise strongly alter the electronic and transport properties. In order to achieve this, we perform a rotation (of 30°) of the ZrS_2 layer in the direction normal to the TMD plane, as illustrated in Fig. 1. Although the dimensions of the resulting supercell are larger than the primitive ones (6.19 Å), it allows minimizing the applied strain values applied to 1.5% for MoS_2 and 1.2% for ZrS_2. In the absence of this rotation, the strain would reach an excessive value of 11%. We then relax the atomic structure, keeping the unit cell constant. Once this process is completed, we compute the band structure to evaluate the effective band gap corresponding to the heterostructures. To analyze the orbital nature of the conduction and valence bands, we perform a projection of the computed wave functions $\psi_{n\vec{k}}(\vec{r})$ at *k* point $\vec{k}$ and band index *n* onto orthogonalized atomic wave functions for each point of the band structure, following

$$\psi_{n\vec{k}}(\vec{r}) = \sum_a A^{\vec{k}}_{an} \phi_{a\vec{k}}(\vec{r}),$$

where the set $\{\phi_{a\vec{k}}(\vec{r})\}$ is composed of the pseudoatomic orbitals read from the GBRV pseudopotentials. The coefficients $A^{\vec{k}}_{an}$ define the *weight* of each orbital in each of the points constituting the band structure.

The Bloch functions of the relaxed stack are then projected onto maximally localized Wannier functions [20] using the WANNIER90 software package [21]. This approach allows building a tight-binding-like Hamiltonian for each configuration which accounts for the interactions up to the sixth nearest neighbors. The ballistic transport properties of the stack are then evaluated using the non-equilibrium Green's-function formalism as implemented in the OMEN package [22]. The building of a device Hamiltonian compatible with the quantum transport solver is performed by generating a rectangular supercell using hexagonal unit cells as building blocks.

We focus on *p*-*i*-*n* TFETs with a channel made of a one-monolayer MoS_2-ZrS_2 heterostructure, controlled by two gates of 10-nm length, separated from the heterostack by 3 nm of HfO_2 (Fig. 2). The equivalent oxide thickness is therefore set to a technologically relevant value of 0.6 nm

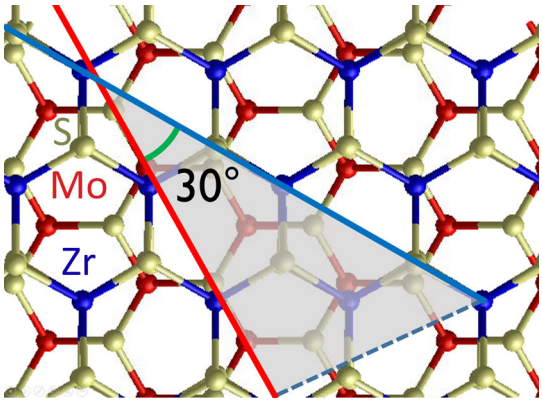

FIG. 1. Atomistic top view of a one-monolayer MoS_2–one-monolayer ZrS_2 heterostructure. The red, blue, and yellow spheres correspond to Mo, Zr, and S atoms, respectively. The angle stresses the rotation applied to the ZrS_2 (30°) about the vector normal to the 2D planes, with respect to the MoS_2 layer.

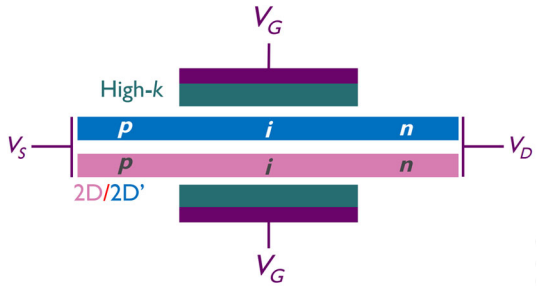

FIG. 2. Schematic view of a TFET built on a van der Waals heterostructure made of two layers. The ideal device contains doped electrodes (a source and a drain) and a *p*-*i*-*n*–doped central region. It is controlled by two gates, isolated from the channel by a high-κ gate dielectric material.

[23], which also ensures a good electrostatic control on the device. The doping concentrations in the electrodes are set to be 6×10^{13} e/cm^2, p type for the source and n type for the drain, in line with the values found in experimental reports [24]. The drain-to-source bias V_{DS} is set to be 0.1 V, to avoid artifacts related to the ballistic transport formalism used. This shortcoming was analyzed by Szabo and coworkers [5], who demonstrated that the negative differential resistance arose from the ballistic formalism [25]. The contribution of gate leakage current is not accounted for in our calculations. For each channel configuration, we compute the transmission spectra and current-voltage characteristics for gate-voltage-bias (V_G) values that range from 0 to 0.35 V. The change in relative positions of the layers is obtained by applying either a translation or a rotation of the ZrS_2 layer with respect to the MoS_2 one. Translations are operated on a 4×4 grid by steps of 0.5 Å along each of the in-plane axes (X and Y). Rotations are performed by steps of 60° and allow us to account for a change in the transport direction in ZrS_2. This is especially important since ZrS_2 has a strongly anisotropic electron effective mass, while MoS_2 has an isotropic one [26].

III. RESULTS AND DISCUSSION

The computed band structure for a MoS_2-ZrS_2 heterostructure is shown in Fig. 3, along with the band alignment. The contributions from the different atomic sites are separated using the methodology described above and are regrouped by layer (being either MoS_2 or ZrS_2). To visualize this contribution, we attribute a coloring scheme to each point of the band structure according to a computed weight, ranging from bright red (wave function being fully localized on MoS_2) to blue (wave function being fully localized on ZrS_2). The diagram stresses that the MoS_2-ZrS_2 heterostructure has an effective band gap of 0.26 eV, whose edges are defined by the valence band of MoS_2 and the conduction band of ZrS_2. This band alignment is close to a broken band gap and in good alignment with previous results reported by Rasmussen and Thygesen [27]. Note, however, that these authors considered isolated layers while in our case, we evaluate the electronic properties of the stacked interacting materials. In the heterostructure, the band gaps of MoS_2 and ZrS_2 are, respectively, 1.80 and 0.97 eV, showing almost no change compared to the value of the isolated monolayer case for MoS_2 and a reduction of 0.1 eV for ZrS_2.

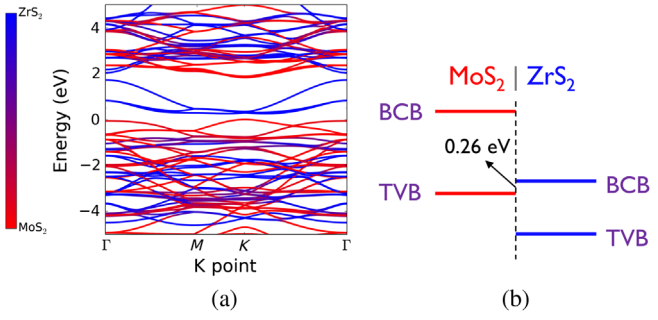

FIG. 3. (a) Band structure of a MoS_2-ZrS_2 heterostructure. The bands are colored in red for MoS_2 and blue for ZrS_2, using projections on atomic orbitals. The top of the valence band is located at the K symmetry point and the bottom of the conduction band is found along the Γ-K symmetry line. (b) Schematic representation of the band alignment computed for the MoS_2-ZrS_2 heterostack.

The examination of the detailed contribution of each atomic orbital in the heterostack reveals that the top of the valence band (TVB) is mainly composed of the p_z orbitals of the S atoms from the MoS_2 layer, while the bottom of the conduction band (BCB) arises from the contribution of the d_{z^2} orbitals of Zr. It is interesting to note that in the heterostructure, the bottom of the conduction band (which is defined by the ZrS_2 layer) is found along the Γ-K symmetry line of the Brillouin zone instead of the Γ-M one as it is the case in isolated ZrS_2 monolayer, with a small energy difference (0.04 eV) separating these two minima. In terms of electron effective mass (illustrated in Fig. 4), these two valleys exhibit fairly different values and anisotropy. In the Γ-K valley, it is strongly anisotropic and spans from $1.26m_0$ to $16.5m_0$, where $m_0 = 9.1 \times 10^{-31}$ kg is the electron mass at rest. In the Γ-M valley, the modulation of the effective mass is less pronounced, going from $0.93m_e$ to $1.82m_0$. This is different from the MoS_2 case, where the effective mass is isotropic.

At the difference with other concepts of TFET devices based on more conventional semiconductor heterostructures (i.e., III-V materials [28]), the main interaction at the heterostructure is defined by weak van der Waals forces.

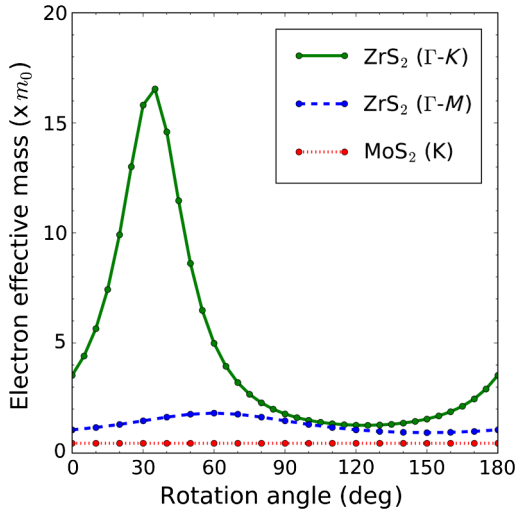

FIG. 4. Evolution of the electron effective masses computed for ZrS_2 for two different conduction band valley minima, one along Γ-K (green, solid), and the other one along Γ-M (dashed) with respect to the transport direction chosen. The electron effective mass for MoS_2 is stressed in comparison as a red dotted line.

In other words, the system has no direct bond between the layers constituting the heterostructure. They can, hence, have some degrees of freedom in their relative orientation or position with respect to each other, given that their interaction energy is weak. Enforcing them into a reproducible stacking pattern can therefore be challenging, especially if the layers are transferred on top of each other during the integration steps of the device. We hence gauged the modulation of the device performances with respect to this variability, accounting for changes in alignment between the layers. We decompose the impact into two components, a translation and a rotation one. The changes in interaction energy at the surface, resulting from these operations ($E_{\text{interaction}}$) are evaluated by the expression

$$E_{\text{interaction}} = \frac{E_{\text{heterostructure}} - (E_{\text{top layer}} + E_{\text{bottom layer}})}{S_{\text{unit cell}}} \quad (\text{in mJ/m}^2),$$

where $S_{\text{unit cell}}$ is the unit cell surface, $E_{\text{heterostructure}}$ is the total energy of the heterostructure, and $E_{\text{top layer}}/E_{\text{bottom layer}}$ are the total energies of the isolated top and bottom layers. Since the interaction energy is driven by the atomic alignment between the layers, we evaluate this expression for two different stacks, accounting for a large mismatch (MoS_2-ZrS_2) and a small one (MoS_2-WS_2). It turns out that the computed values are, respectively, 176 mJ/m^2 and 336 mJ/m^2, and lie within the reported typical order of magnitude for van der Waals interactions, such as in MoS_2 [29] and WS_2 [30]. Whenever the lattice parameters of the stack layers are similar, as it is the case for MoS_2-WS_2, the layers interact more significantly. Our simulations reveal that in the MoS_2-ZrS_2 heterostructure, the total energy evolves weakly, with variations inferior to 10 mJ/m^2 upon translations and rotations (Fig. 5). This observation suggests that there is little thermodynamic driving force that could favor a specific orientation for the heterostacks. In contrast, for stacks made of materials with similar lattice parameters, such as MoS_2-WS_2, the interaction between the layers is enhanced and variations in energy larger than 100 mJ/m^2 are observed (Fig. 5). In this case, the heterostructure tends to adopt a preferential (*AA*', for instance) stacking pattern. The electronic properties of the MoS_2-ZrS_2 stack are found to be unaltered by relative translations and rotations of the layers, with changes in the band gap and offsets lower than 0.01 eV.

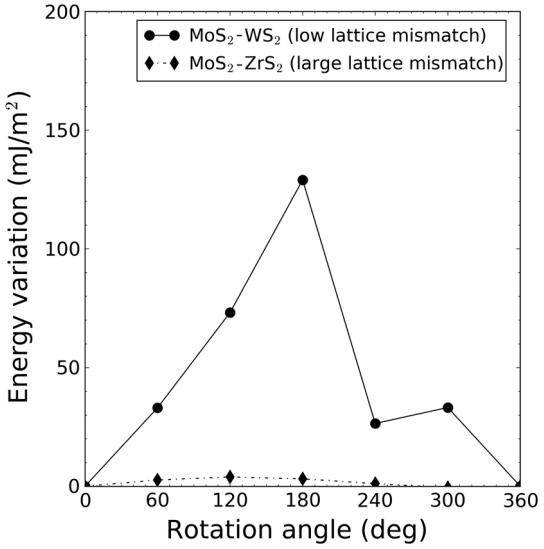

FIG. 5. Change in total energy with respect to the rotation angle applied to the layer in contact with MoS_2.

The simulations of the device characteristics reveal that the performances of the MoS_2-ZrS_2 TFET are attractive in terms of the $I_{\text{on}}/I_{\text{off}}$ ratio with ~8 orders of magnitude of variation in the drive current, and a steep subthreshold swing of 16 mV/dec, as shown by the red curve in Fig. 6. The *on* current (~10 μA/μm) is comparable to the values reported for state-of-the-art TFET devices made of traditional 3D semiconductors [31]. Therefore, the combination of this relatively large *on* current with the steep subthreshold slope makes this device very promising for low-power applications. However, we also observe a variability (around one order of magnitude) upon translations and rotations of the ZrS_2 layer with respect to the MoS_2 one. Given that the MoS_2-ZrS_2 heterostructure has a close-to-broken band-gap alignment, a band-to-band tunneling current is expected to take place upon the electrostatic modulation of a gate, between the TVB of MoS_2 (Fig. 3, red) and the BCB of ZrS_2 (Fig. 3, blue). Therefore,

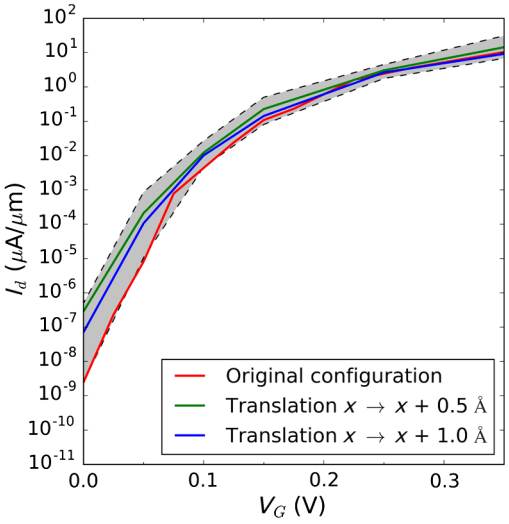

FIG. 6. Current-voltage characteristics in a MoS_2-ZrS_2 TFET (red solid curve). The gray shaded area depicts the range of current values observed in all the tested configurations, which include translation and rotation operations applied on the ZrS_2 monolayer. To illustrate the variability in current, the current-voltage characteristics are also shown for two other configurations, obtained by a translation of the ZrS_2 layer by 0.5 Å (green) and 1 Å (blue).

both the transport direction (due to the anisotropic effective mass in ZrS_2) and the overlap between those orbitals should play a central role in this out-of-plane tunneling process.

To obtain insight into the tunneling current and its variability with respect to the transport direction, we first consider the expression of the tunneling current density J provided by the Wentzel-Kramers-Brillouin approximation, while assuming that the potential barrier adopts a triangular shape [32]:

$$J = \frac{\sqrt{2m_R^*}q^3FV_R}{8\pi^2\hbar^2E_G^{1/2}}\exp\left(-\frac{4\sqrt{2m_R^*}E_G^{3/2}}{3qF\hbar}\right),$$

where $m_R^* = [(1/m_e^*) + (1/m_h^*)]^{-1}$ is the reduced effective mass, m_e^* is the electron effective mass (corresponding to the ZrS_2 layer), m_h^* is the hole one (MoS_2 layer), $\hbar$ is the reduced Planck constant, q is the charge of the electron, E_G is the effective band gap, V_R is the reverse bias, and F is the maximum electric field in the junction (here, at the p-i boundary). For 2D materials, an analogous expression was derived by Jena [33]:

$$J^{2D} = \frac{qg_cg_v\sqrt{2m_R^*\bar{E}}}{2\pi^2\hbar^2}T_0\left[(qV-\bar{E})\sqrt{\pi}\,\mathrm{erf}\left(\sqrt{\frac{qV}{2\bar{E}}}\right) + \sqrt{qV\times 2\bar{E}}\exp\left(-\frac{qV}{2\bar{E}}\right)\right],$$

where $g_s = 2$ is the spin degeneracy, g_v is the valley degeneracy, $\mathrm{erf}(x) = (2/\sqrt{\pi})\int_0^x e^{-t^2}dt$ is the error function, $\bar{E} = q\hbar F/2\sqrt{2m_R^*E_G}$, and $T_0 = \exp(-4\sqrt{2m_R^*}E_G^{3/2}/3q\hbar F)$. By changing the transport direction, only the electron effective mass of ZrS_2 is impacted, leading to a modulation of the reduced effective mass (m_R^*) while the hole effective mass of MoS_2 remains at $0.56m_0$. Near the *off* state (at low V_G), only the Γ-K valley is populated, with a direction-dependent electron effective mass varying from $1.26m_0$ to $16.5m_0$, so m_R^* varies from $0.39m_0$ to $0.54m_0$. In the *on* state (high V_G), the Γ-M valley is also populated and becomes dominant. Its electron effective mass varies from $0.93m_0$ to $1.82m_0$. This reduces the m_R^* variations, which go from $0.35m_0$ to $0.43m_0$ and, therefore, leads to a weaker impact on the interband tunneling current. Assuming an electric field of 5 V/nm and a band gap of 0.26 eV, we find that the current varies by 15% whenever the Γ-K valley is used while for the Γ-M one, it varies by only 9% in the Γ-M valley upon rotation. This, however, cannot explain by itself the large variations computed in our first-principles and quantum transport calculations reported in Fig, 6 upon translation and rotation operations.

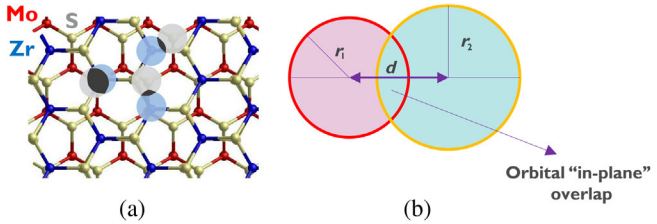

FIG. 7. Illustration of the method used to compute the simplified orbital overlap between the layers. (a) Atomic configuration on which disks of radii 0.5 Å are sketched around the S atoms of MoS_2 (light gray) and the Zr ones in ZrS_2 (blue). The intercepting area of the two surfaces, colored in dark gray, provides the total simplified orbital overlap corresponding to the atomic configuration chosen for the stack. (b) The overlap area is computed by the overlap of each pair of disks of different colors.

As mentioned above, the overlap between the p_z (S from MoS_2) and d_{z^2} (Zr) orbitals are expected to have a significant impact in the tunneling process. To quantify it, we adopt a simplified approach that consists of evaluating the intersection of the p_z and d_{z^2} orbitals between the layers through a two-dimensional projection. Given the shape of the p_z and d_{z^2} orbitals, their projections onto the atomic plane is circular. We, hence, approximate the orbital overlap between the wave functions of the layers active in the transfer process by evaluating the overlay cross sections between the projected orbitals. This consists of determining the intersection between two disks for each pair of projected orbitals in the different layers on the atomic sites of interest. The radii of the cross sections are arbitrarily set to be 0.5 Å. This simplified approach allows the evaluation of a first-order approximation of the *orbital overlap* between the TVB from the MoS_2 layer and the BCB from the ZrS_2 one for each configuration of the stack, as illustrated in Fig. 7. The overlap S_{ij} for a pair of atoms (i, j) between two disks of radii r_1 and r_2, separated by a center-to-center distance d, within the boundaries $0 < d \le r_1 + r_2$ takes the form

$$S_{ij} = \frac{1}{2}\sqrt{(d+r_1+r_2)(-d+r_1+r_2)(d+r_1-r_2)(d-r_1+r_2)}.$$

To understand the possible impact of topology on the device properties' variability and on the factors driving it, we compare the resulting drive current for two different gate bias values, at 0.05 and 0.35 V, which correspond to the potentials needed to obtain a steep region and an *on* region, respectively.

At $V_G = 0.35$ V, the space-resolved local density-of-states profile and the transmission spectrum (Fig. 8) reveal

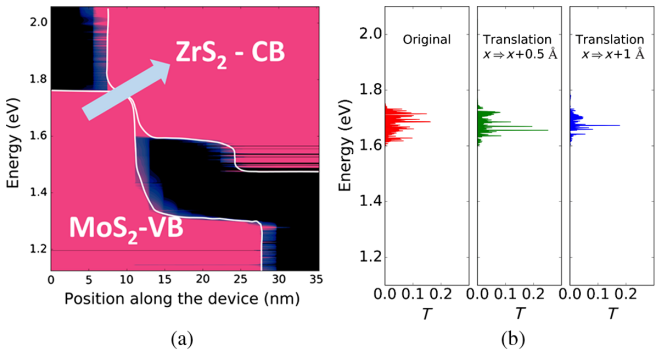

FIG. 8. (a) Spatially resolved local density of states (LDOS) computed along the same device for an energy range of 1 eV at $V_G = 0.35$ V (*on* state). (b) Transmission spectra corresponding to the *I*-*V* curves shown in Fig. 6 for the same energy values as in the LDOS profile. Also shown are the transmission spectra for two other configurations obtained by a translation of the ZrS_2 layer by 0.5 Å (green) and 1 Å (blue). The computed drive-current densities in the three configurations are 14.6, 14.4, and 9.2 μA/μm, corresponding to the red, green, and blue curves, respectively.

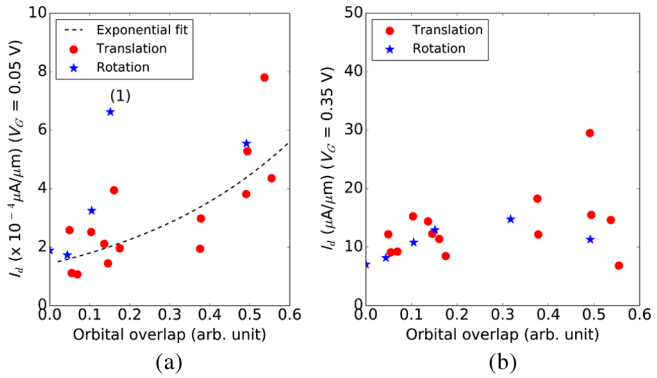

FIG. 9. Drive current at (a) $V_G = 0.05$ V and (b) at $V_G = 0.35$ V for different stack configurations obtained by translations and rotations of the ZrS_2 layer with respect to the MoS_2 one. The x axis reports the computed simplified orbital overlap. Configurations obtained by translation (rotation) are shown in red, small dots (blue, stars). An exponential fit is drawn to underline the correlation between the current and the orbital overlap.

that the main component of the current is dominated by a band-to-band tunneling process occurring between the TVB of MoS_2 (from the sulfur atoms) and the BCB of ZrS_2 (from the zirconium atoms). This tunneling process at the origin of the steep subthreshold switching of the device and the computed transmission profiles are similar to the ones reported by Szabo *et al.* for a $MoTe_2$-SnS_2 TFET device concept [13]. This is also confirmed by the position and the sharpness of the transmission peak, which occur in the narrow energy range corresponding to the region where the conduction band of ZrS_2 falls below the valence band of MoS_2 ([1.6,1.75] eV) due to the applied gate bias. Interestingly, the translation of the ZrS_2 layer by 0.5 and 1 Å along the x axis leads to a change in both the transmission peak positions and intensities, which hints at a modulation of the interaction between the layers and, hence, to a change in the device behavior. For these three configurations, the resulting current density values are, respectively, 14.6, 14.4, and 9.2 μA/μm.

Whenever the layers are rotated or translated with respect to each other, the *off* and *on* currents, as well as the SS are significantly modulated (Fig. 6, shaded area). Close to the off state [Fig. 9(a)], the current varies with a 15-to-1 ratio, depending on the configuration adopted. Interestingly, in the case of the translated layers, there is a clear correlation between the intensity of the current and the computed orbital overlap, highlighting the importance of the band-to-band tunneling component and its dependence on the relative positions of the layers [Fig. 9(a)]. Upon rotation operations, certain current points appear to lie within the variations obtained upon translations, while other ones lie outside the distribution [see label (1) in Fig. 9(a)]. We attribute this deviation to the modulation of the anisotropic electron effective mass of ZrS_2 along the Γ-K valley (Fig. 4).

The dependence on the orbital overlap between the layers appears to be less pronounced for the *on* state. Further, at high V_G values, the conduction valley along Γ-M also becomes populated and dominant in the device operation, consistently with the band structure shown in Fig. 3, where a small difference of 0.04 eV exists between the two minima. In this valley, the electron effective mass is more isotropic than in along the Γ-K symmetry line, with a modulation going from $0.93m_e$ to $1.82m_0$ (Fig. 4).

In conclusion, the combination of these effects on the *on* and *off* currents leads to a modulation of the *on*:*off* ratio from 6×10^6 to 9×10^8 and to a distribution of the SS that spans from 10 mV/dec to 26 mV/dec.

IV. CONCLUSIONS

Our ballistic quantum transport simulations, based on first-principles Hamiltonians projected onto a Wannier basis, suggest that MoS_2-ZrS_2 is a promising material combination to develop a TFET device with a subthreshold swing below 20 mV/dec and a large *on*:*off* current ratio. Despite the apparent invariance of the band structure with respect to the alignment of the layers, our findings also indicate that a variability exists in the tunneling current, which depends on both the interlayer orbital overlap and on the transport direction. Both the *on*:*off* ratio and subthreshold slope are found to be strongly impacted. Our study stresses the fact that 2D materials used to build a heterostack for TFET application should not only meet the requirements in terms of a (close to) broken band-gap alignment but also that the two materials should have similar lattice properties to favor a controlled specific relative orientation of the layers and hence to reduce the

variability induced by changes in their relative alignment. Therefore, adopting a heterostack built on $MoTe_2$-SnS_2, $MoTe_2$-ZrS_2, or HfS_2-$SnSe_2$ could help with enforcing the alignment, thus reducing the variability.

ACKNOWLEDGMENTS

The computational resources and services used in this work were provided by the VSC (Flemish Supercomputer Center), funded by the Research Foundation–Flanders (FWO) and the Flemish Government–Department EWI.

[1] M. Luisier, M. Lundstrom, D. A. Antoniadis, and J. Bokor, in *Proceedings of the Electron Devices Meeting (IEDM)* (IEEE, Washington, DC, 2011).

[2] M. Leong, B. Doris, J. Kedzierski, and Yang Min, Silicon device scaling to the sub-10-nm regime, Science **306**, 2057 (2004).

[3] K. S. Novoselov, A. K. Geim, S. V. Morozov, D. Jiang, Y. Zhang, S. V. Dubonos, I. V. Grigorieva, and A. A. Firsov, Electric field effect in atomically thin carbon films, Science **306**, 666 (2004)

[4] B. Radisavljevic, A. Radenovic, J. Brivio, V. Giacometti, and A. Kis, Single-layer MoS_2 transistors, Nat. Nanotechnol. **6**, 147 (2011).

[5] A. Szabo, R. Rhyner, and M. Luisier, *Ab initio* simulation of single- and few-layer MoS_2 transistors: Effect of electron-phonon scattering, Phys. Rev. B **92**, 035435 (2015).

[6] S. Datta, *Quantum Transport: Atom to Transistor* (Cambridge University Press, Cambridge, U.K., 2013).

[7] A. S. Verhulst, W. G. Vandenberghe, K. Maex, and G. Groeseneken, Tunnel field-effect transistor without gate-drain overlap, Appl. Phys. Lett. **91**, 053102 (2007).

[8] H. Ilatikhameneh, Y. Tan, B. Novakovic, G. Klimeck, R. Rahman, and J. Appenzeller, Tunnel field-effect transistors in 2-D transition metal dichalcogenide materials, IEEE J. Explor. Solid-State Comput. Devices Circuits **1**, 12 (2015).

[9] H. Ilatikhameneh, T. A. Ameen, G. Klimeck, J. Appenzeller, and R. Rahman, Dielectric engineered tunnel field-effect transistor, IEEE Electron Device Lett. **36**, 1097 (2015).

[10] A. K. Geim and I. V. Grigorieva, Van der Waals heterostructures, Nature (London) **499**, 419 (2013).

[11] A. K. A. Lu, M. Houssa, I. Radu, and G. Pourtois, Toward an understanding of the electric field-induced electrostatic doping in van der Waals heterostructures: A first-principles study, ACS Appl. Mater. Interfaces **9**, 7725 (2017).

[12] C. Gong, H. Zhang, W. Wang, L. Colombo, R. M. Wallace, and K. Cho, Band alignment of two-dimensional transition metal dichalcogenides: Application in tunnel field effect transistors, Appl. Phys. Lett. **103**, 053513 (2013).

[13] A. Szabo, S. J. Koester, and M. Luisier, *Ab-initio* simulations of van der Waals; $MoTe_2$-SnS_2 heterotunneling FETs for low-power electronics, IEEE Electron Device Lett. **36**, 514 (2015).

[14] Q. Yuanju, P. Hui, and K. Chi Tat, Hydrogenation-controlled phase transition on two-dimensional transition metal dichalcogenides and their unique physical and catalytic properties, Sci. Rep. **6**, 34186 (2016).

[15] J. Klimeš, D. R. Bowler, and A. Michaelides, Van der Waals density functionals applied to solids, Phys. Rev. B **83**, 195131 (2011).

[16] S. Grimme, Semiempirical GGA-type density functional constructed with a long-range dispersion correction, J. Comput. Chem. **27**, 1787 (2006).

[17] P. Giannozzi *et al.*, QUANTUM ESPRESSO: A modular and open-source software project for quantum simulations of materials, J. Phys. Condens. Matter **21**, 395502 (2009).

[18] H. J. Monkhorst and J. D. Pack, Special points for Brillouin-zone integrations, Phys. Rev. B **13**, 5188 (1976).

[19] K. F. Garrity, J. W. Bennett, K. M. Rabe, and D. Vanderbilt, Pseudopotentials for high-throughput DFT calculations, Comput. Mater. Sci. **81**, 446 (2014).

[20] N. Marzari and D. Vanderbilt, Maximally localized generalized Wannier functions for composite energy bands, Phys. Rev. B **56**, 12847 (1997).

[21] A. A. Mostofi, J. R. Yates, G. Pizzi, Y.-S. Lee, I. Souza, D. Vanderbilt, and N. Marzari, An updated version of WANNIER90: A tool for obtaining maximally-localised Wannier functions, Comput. Phys. Commun. **185**, 2309 (2014).

[22] M. Luisier, A. Schenk, W. Fichtner, and G. Klimeck, Atomistic simulation of nanowires in the $sp^3d^5s^*$ tight-binding formalism: From boundary conditions to strain calculations, Phys. Rev. B **74**, 205323 (2006).

[23] J.-H. Ahn and S.-H. Kwon, Sub-0.5 nm equivalent oxide thickness scaling for Si-doped $Zr_{1-x}Hf_xO_2$ thin film without using noble metal electrode, ACS Appl. Mater. Interfaces **7**, 15587 (2015).

[24] A. Tarasov, S. Zhang, M.-Y. Tsai, P. M. Campbell, S. Graham, S. Barlow, S. R. Marder, and E. M. Vogel, Controlled doping of large-area trilayer MoS_2 with molecular reductants and oxidants, Adv. Mater. **27**, 1175 (2015).

[25] J. Chang, L. F. Register, and S. K. Banerjee, Atomistic full-band simulations of monolayer MoS_2 transistors, Appl. Phys. Lett. **103**, 223509 (2013).

[26] P. Miro, M. Audiffred, and T. Heine, An atlas of two-dimensional materials, Chem. Soc. Rev. **43**, 6537 (2014).

[27] F. A. Rasmussen and K. S. Thygesen, Computational 2D materials database: Electronic structure of transition-metal dichalcogenides and oxides, J. Phys. Chem. C **119**, 13169 (2015).

[28] E. Lind, E. Memisevic, A. W. Dey, and L.-E. Wernersson, III-V heterostructure nanowire tunnel FETs, J. Electron Devices Soc. **3**, 96 (2015).

[29] S.-L. Shang, G. Lindwall, Y. Wang, J. M. Redwing, T. Anderson, and W.-K. Liu, Lateral versus vertical growth of two-dimensional layered transition-metal dichalcogenides: Thermodynamic insight into MoS_2, Nano Lett. **16**, 5742 (2016).

[30] G. V. Bianco, M. Losurdo, M. M. Giangregorio, A. Sacchetti, P. Prete, N. Lovergine, P. Capezzuto, and B. Bruno, Direct epitaxial CVD synthesis of tungsten disulfide on epitaxial and CVD graphene, RSC Adv. **5**, 98700 (2015).

[31] H. Lu and A. Seabaugh, Tunnel field-effect transistors: State-of-the-art, IEEE J. Electron Devices Soc. **2**, 44 (2014).

[32] A. C. Seabaugh and Q. Zhang, Low-voltage tunnel transistors for beyond CMOS logic, Proc. IEEE **98**, 2095 (2010).

[33] D. Jena, Tunneling transistors based on graphene and 2-D crystals, Proc. IEEE **101**, 1585 (2013).